Porin self-association enables cell-to-cell contact in Providencia stuartii floating communities

Mariam El Khatib, Chady Nasrallah, Julie Lopes, Que-Tien Tran, Guillaume Tetreau, Hind Basbous, Daphna Fenel, Benoit Gallet, Mathilde Lethier, Jean-Michel Bolla, et al.

Porin self-association enables cell-to-cell contact in *Providencia stuartii* floating communities

Mariam El-Khatib[a,1], Chady Nasrallah[a,1,2], Julie Lopes[a], Que-Tien Tran[b], Guillaume Tetreau[a], Hind Basbous[a], Daphna Fenel[a], Benoit Gallet[a], Mathilde Lethier[a], Jean-Michel Bolla[c], Jean-Marie Pagès[c], Michel Vivaudou[a,d], Martin Weik[a], Mathias Winterhalter[b], and Jacques-Philippe Colletier[a,3]

[a]Institut de Biologie Structurale (IBS), University of Grenoble Alpes (UGA), Centre National de la Recherche Scientifique (CNRS), Commissariat à l'énergie atomique et aux énergies alternatives (CEA), 38000 Grenoble, France; [b]Life Sciences & Chemistry, Jacobs University, 28759 Bremen, Germany; [c]UMR MD1, Aix-Marseille University, Institut de Recherche Biomédicale des Armées, Marseille, F-13385 Marseille, France; and [d]Laboratories of Excellence, Ion Channel Science and Therapeutics, 06560 Valbonne, France

Edited by Robert M. Stroud, University of California, San Francisco, CA, and approved January 31, 2018 (received for review August 18, 2017)

The gram-negative pathogen *Providencia stuartii* forms floating communities within which adjacent cells are in apparent contact, before depositing as canonical surface-attached biofilms. Because porins are the most abundant proteins in the outer membrane of gram-negative bacteria, we hypothesized that they could be involved in cell-to-cell contact and undertook a structure-function relationship study on the two porins of *P. stuartii*, Omp-Pst1 and Omp-Pst2. Our crystal structures reveal that these porins can self-associate through their extracellular loops, forming dimers of trimers (DOTs) that could enable cell-to-cell contact within floating communities. Support for this hypothesis was obtained by studying the porin-dependent aggregation of liposomes and model cells. The observation that facing channels are open in the two porin structures suggests that DOTs could not only promote cell-to-cell contact but also contribute to intercellular communication.

biofilms | porins | intercellular communication | cell adhesion | steric zippers

The opportunistic pathogen *Providencia stuartii*, from the Enterobacteriaceae family (1), is involved in increasingly frequent infections in burn victims and patients undergoing long-term catheterization (2–5). Treatment of infections by *P. stuartii* is complicated by its intrinsically strong resistance to a wide range of antibiotics (4, 6–8) and by its ability to form biofilms. The latter may attach and grow on indwelling catheters (3, 9, 10) and on uroepithelial cells (11). Recently, we reported the microscopic characterization of *P. stuartii* plankton and biofilms and the unexpected finding that this species forms floating communities of cells in solution before its deposition as a surface-attached biofilm (12). Within floating communities, cells are in apparent contact and presumably stick to one another via protein–protein interactions (12). Inasmuch as the general diffusion porins are the most abundant proteins in the outer membrane (OM) of gram-negative bacteria, with a major porin often accounting for up to 70% of the OM protein content (up to 10^5 copies per cell) (13), we set out to verify whether *P. stuartii* porins could partake in the formation of floating communities.

Porins are water-filled channels spanning the OM of gram-negative bacteria (14) and constitute the principal entry route for hydrophilic nutrients, ions, and antibiotics into the periplasm. They are generally assembled as trimers, within which each monomer displays a conserved β-stranded architecture that delineates a hydrophilic channel. Substrate-specific porins are barrels of 18 β-strands, while porins governed by general diffusion (referred to as porins throughout the manuscript) feature 16 β-strands. In both cases, sifting properties are determined by the amino acid distribution at their constriction zone, contributed by the folding of extracellular loop L3 into the channel lumen. The genome of *P. stuartii* encodes two porins, Omp-Pst1 and Omp-Pst2. The uptake of β-lactams (cephalosporins and carbapenems, in particular), quinolones, and fluoroquinolones is mainly due to their passive diffusion through Omp-Pst1 (6, 7). Omp-Pst1 is essential to *P. stuartii* survival, while Omp-Pst2 promotes rapid growth, possibly through regulation of the cationic content of the periplasm (12).

To obtain insight into how Omp-Pst1 and Omp-Pst2 could be linked to the pathogenicity of *P. stuartii*, we first determined their 3D structures. These reveal the molecular basis for the distinct ion selectivity of Omp-Pst1 and Omp-Pst2, while that of a complex with maltose suggests an involvement of Omp-Pst1 in carbohydrate harvesting and uptake. Analysis of crystal-packing interactions led to the discovery of an oligomeric assembly common to both porins and formed by the face-to-face association of two porin trimers through their extracellular loops. These dimers of trimers (DOTs) assemble through steric zipper interactions between homo-specific segments. Incorporation of either of the porins into liposomes results in proteoliposome aggregation, while their ectopic expression in a porin-devoid *Escherichia coli* strain induces a shift from the state of isolated plankton to that of floating communities. Thus, our results support the hypothesis that porins contribute to cell-to-cell contact in floating communities of *P. stuartii* (12). We propose that DOTs are the biological assemblies at the basis of

Significance

We report that porins, the main gateway for hydrophilic nutrients and ions into bacterial cells, assemble face-to-face in crystals, yielding dimers of trimers (DOTs). Further investigation suggests that DOTs could support cell-to-cell contact in the floating communities formed by *Providencia stuartii*, and could enable direct communication between adjacent cells. Self-matching steric zipper interactions are observed at the dimer interface, suggesting a means by which DOT formation could be restricted to cells of the same clonal origin.

Author contributions: M.E.-K., C.N., and J.-P.C. designed research; M.E.-K., C.N., J.L., Q.-T.T., G.T., H.B., D.F., B.G., M.L., and J.-P.C. performed research; Q.-T.T., G.T., J.-M.B., J.-M.P., M.V., M. Weik, and M. Winterhalter contributed new reagents/analytic tools; M.E.-K., C.N., J.L., G.T., M.V., M. Weik, and J.-P.C. analyzed data; and M.V. and J.-P.C. wrote the paper with input from M.E.-K., C.N., J.L., Q.-T.T., G.T., J.-M.P., M. Weik, and M. Winterhalter.

The authors declare no conflict of interest.

This article is a PNAS Direct Submission.

Data deposition: The atomic coordinates and structure factors have been deposited in the Protein Data Bank, www.wwpdb.org, under the following PDB accession codes: Omp-Pst1 type-A (4d64), Omp-Pst1 type-B (5nxr), maltose complex with Omp-Pst1 type-B (5nxu), Omp-Pst2 (4d65), 283-LGNY-286 (5n9i), 206-GVVTSE-211 (5n9h), and Omp-Pst1-Δ207-216-N293G (5nxn).

[1]M.E.-K. and C.N. contributed equally to this work.

[2]Present address: UMR 5203, Institut de Génomique Fonctionnelle, F-34094 Montpellier, France.

[3]To whom correspondence should be addressed. Email: colletier@ibs.fr.

This article contains supporting information online at www.pnas.org/lookup/suppl/doi:10.1073/pnas.1714582115/-/DCSupplemental.

Published online February 23, 2018.

the cell-to-cell contact property and that they could provide a means of direct communication between cells.

Results

Structures of Omp-Pst1 and Its Complex with Maltose. The structure of native Omp-Pst1 was solved in two space groups: C2 (type A; 3.2 Å resolution) and $P2_12_12_1$ (type B; 2.7 Å resolution) (*SI Appendix*, Table S1). In both crystal forms, the asymmetric unit contains a single trimer. In type A crystals, dimerization of trimers along the crystallographic twofold axis results in a DOT, assembled through steric zipper interactions between homologous segments in facing extracellular loops (Fig. 1*A*). In type B crystals, contact is also observed between extracellular loops but does not involve self-matching interactions. In both types of crystals, no contact is observed between intracellular turns, and complementary contact is established between transmembrane regions. The trimeric structures of Omp-Pst1 in type A and type B crystals are similar, superimposing with an rmsd of 0.356 Å over 1,056 residues. While extracellular loops of Omp-Pst1 are mostly folded as α-helices, the L5 extracellular loop of each monomer contributes a β-hairpin that is positioned over the channel's extracellular vestibule and complicates access to the pore (*SI Appendix*, Fig. S1*A*). In type A crystals, the L5 β-hairpins are additionally involved in the crystal-packing interactions that underlie DOT assembly, at the unit cell level (Fig. 1 *A* and *B*).

Compared with the canonical porins OmpF, OmpC, and PhoE from *E. coli*, Omp-Pst1 displays a similar pattern of charge distribution. In particular, the Omp-Pst1 channel is positively charged (+5e in Omp-Pst1 vs. +3e, +3e, and +6e in OmpF, OmpC, and PhoE, respectively) (Fig. 1*I* and *SI Appendix*, Fig. S2*A*), with a net

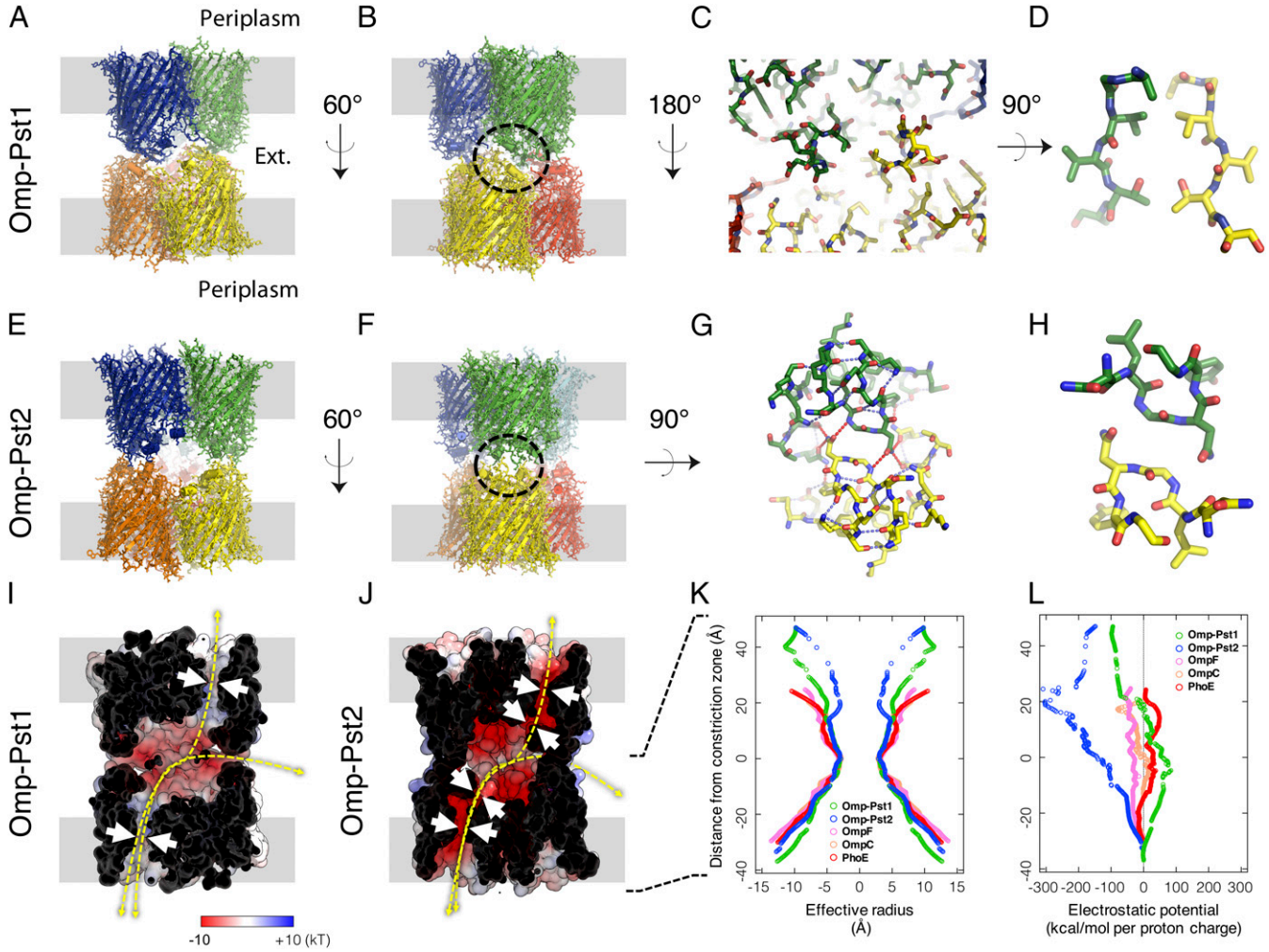

Fig. 1. Omp-Pst1 and Omp-Pst2 form DOTs. (*A*) Lateral view of the Omp-Pst1 DOT. The presumed positions of OMs are shown in gray. (*B*) Same view after 60° vertical rotation. (*C*) Interaction region (circled in *B*) between facing monomers. (*D*) Enlarged view of the center of *C* showing a symmetry class III steric zipper that is buried in the core of the DOT structure. (*E*–*H*) Equivalent views of the Omp-Pst2 DOT. Main differences are the ellipsoidal fenestrations evident in *E* and the presence of a symmetry class I steric zipper in *H*. (*I*) The dimerization interface of the Omp-Pst1 DOT, viewed as in *B*, delineates a large negatively charged cavity. The electrostatic potential is mapped on the solvent-accessible surface. (*J*) Equivalent representation of Omp-Pst2. In *I* and *J*, white arrows indicate constrictions along the porin channels, whereas yellow arrows indicate possible translocation pathways across porin DOTs: between the periplasm of two adjacent cells, along porin channels, or between the periplasmic space of each cell and the external medium, through fenestrations of the DOTs. (*K*) Effective radii measured along Omp-Pst1 (green), Omp-Pst2 (blue), and *E. coli* porin channels using a 1-Å positively charged rolling probe (equivalent to a proton). The *y* axis indicates vertical position along the channels from periplasmic (positive *y* values) to extracellular (negative *y* values) ends, with reference to the central constriction zone ($z = 0$) contributed by L3. Channels of Omp-Pst1, Omp-Pst2, and *E. coli* porins all display similar radii at their central constriction zone, but the Omp-Pst2 channel features an additional constriction zone in its extracellular vestibule. (*L*) Equivalent plots of electrostatic potentials associated with the translocation of a proton, indicating that Omp-Pst1 is mildly anion selective, while Omp-Pst2 is strongly cation selective. The energy profile of Omp-Pst2 further suggests a facilitated transport of cations from the periplasm to the external medium.

charge of +1e at the constriction zone (0e, −2e, and 0e in OmpF, OmpC, and PhoE, respectively) (Fig. 1 *K* and *L* and *SI Appendix*, Fig. S2*B*). The electrostatic potential profile calculated along the channel of Omp-Pst1 indicates mild anion selectivity (Fig. 1*L*), in line with electrophysiology measurements and with molecular dynamics (MD) simulations based on this structure (15). Nevertheless, the Omp-Pst1 channel features more charged residues than *E. coli* porins (48%, 35%, and 20% more charged residues than OmpF, OmpC, and PhoE, respectively), suggesting higher translocation selectivity. The extracellular vestibule of Omp-Pst1 is negatively charged (Fig. 1 *I* and *L*).

In an attempt to determine whether or not Omp-Pst1 is involved in translocation of uncharged nutrients into the periplasm, a structure of a complex with maltose was obtained by soaking type B crystals in a mother liquor solution containing 100 mM maltose. The structure of the complex indicates electron density for three maltose molecules, that is, one per monomer, at an identical binding site. Specifically, residues from extracellular loops L1 (K31, E33), L3 (Q121), L6 (R251, G253), L7 (L300), and L8 (G337, N339) form a groove above the constriction zone within which each maltose establishes six to eight H-bonds (depending on the monomer), burying around 70% of its accessible surface (*SI Appendix*, Fig. S1*B*). The presence of a tight binding site at the channel entrance could underlie a role for Omp-Pst1 in the facilitated translocation of carbohydrates. Ensemble refinement of the maltose-bound Omp-Pst1 structure reveals increased dynamics in L3 residue D117, positioned below the maltose binding site and above the channel constriction zone (*SI Appendix*, Fig. S1*B*). Hence, D117 could participate in the translocation of maltose from its binding site in the extracellular vestibule to the periplasmic side. Moreover, in all Omp-Pst1 structures, a Ca^{2+} ion could be modeled at the interfacial cavity between the three monomers of the trimer, stabilized by cation-π interaction with the side chain of Trp62 from each monomer (*SI Appendix*, Fig. S3 *A* and *B*). Interestingly, this central cavity is opened to the intracellular side but is closed at the extracellular side by symmetrical interactions between Asn75 side chains from the three monomers. Substitution of Ca^{2+} by exposure of the porin to high Zn^{2+} concentrations leads to a dissociation of the trimer, suggesting that this channel-buried ion binding site could be involved in the regulation of Omp-Pst1 oligomerization (*SI Appendix*, Fig. S3*C*).

Structure of Omp-Pst2. The structure of Omp-Pst2 was solved in the $P2_1$ space group at 2.2 Å resolution (*SI Appendix*, Table S1). A DOT is observed in the asymmetric unit formed by the face-to-face, self-matching interaction of two trimers through their extracellular loops (Fig. 1 *E* and *F*). Hence, Omp-Pst2 and type A Omp-Pst1 crystals reveal a similar biological assembly (Fig. 1 *A*, *B*, *E*, and *F*). The extracellular loops of Omp-Pst2 are mostly folded as α-helices (*SI Appendix*, Fig. S1*C*), thus contributing an additional constriction zone at the entrance of the channel, which could affect the diffusion of large solutes across Omp-Pst2 (Fig. 1 *J* and *K*). Compared with *E. coli* OmpF, OmpC, and PhoE, the Omp-Pst2 channel features a similar amount of charged residues (20% more charged residues than OmpF, and 8% and 4% less than OmpC and PhoE, respectively) but has a characteristic pronounced acidic nature (Fig. 1*L* and *SI Appendix*, Fig. S2*C*). The net charge of Omp-Pst2 channel is indeed −4e at the constriction zone, suggesting a strong cation selectivity (Fig. 1*L* and *SI Appendix*, Fig. S2*D*), which has been verified by electrophysiology measurements (15). Calculation of the electrostatic potential along the Omp-Pst2 channel furthermore suggests a facilitated transport of cations from the intracellular to the extracellular side of the porin (Fig. 1 *J* and *L*), in line with recent MD simulations based on the structure (15). We note that as in Omp-Pst1 crystals, no contact is observed between intracellular turns of Omp-Pst2, and a cavity is apparent at the center of the trimeric complex. This cavity is open at its intracellular end but insulated from the extracellular bulk by symmetrical interactions between Asn72 (equivalent to Omp-Pst1 Asn75) side chains from the three monomers. At the top of this cavity, an SO_4^{2-} was modeled which appears to be stabilized by an anion-π interaction with the side chain of Trp59 from each monomer (*SI Appendix*, Fig. S3 *E* and *F*). Similar to Omp-Pst1, exposure of Omp-Pst2 to high Zn^{2+} concentrations leads to a dissociation of the trimer, suggesting a critical role for this central ion binding site in the regulation of Omp-Pst2 oligomerization (*SI Appendix*, Fig. S3 *C* and *D*). Furthermore, it shows that the central channel of Omp-Pst2 can accommodate both positively charged and negatively charged divalent ions.

Omp-Pst1 and Omp-Pst2 Form DOTs Assembled Through Steric Zipper Interactions. In Omp-Pst2 and in type A Omp-Pst1 crystals, packing is supported by the face-to-face interaction of two trimers via their extracellular loops, yielding DOTs (Fig. 1 *A*, *B*, *E*, and *F*). In both DOTs, the dimerization interface delineates a large negatively charged cavity (volumes of 30,610 and 37,959 $Å^3$ for Omp-Pst1 and Omp-Pst2, respectively) (Fig. 1 *I* and *J*). The cavity of Omp-Pst2 is accessible from the bulk via three ellipsoidal fenestrations of 17 × 29 Å (Fig. 1 *E*, *F*, and *J*), while that of Omp-Pst1 is shielded from the bulk and presumably only accessible to water (Fig. 1 *A*, *B*, and *I*). The buried surface areas per facing trimer are 921 $Å^2$ for Omp-Pst1 and 1,215 $Å^2$ for Omp-Pst2 DOTs—that is, values above the threshold of 856 $Å^2$ that has been proposed to discriminate between artificial and biological dimers in crystal structures (16). In comparison, the buried surface area per facing trimer is 350 $Å^2$ in type B Omp-Pst1 crystals. The surface complementarity between facing trimers of the DOT is 0.40 for Omp-Pst1 and 0.64 for Omp-Pst2. The latter value is close to that displayed by antibody–antigen complexes, namely 0.65 (17).

The DOTs formed by Omp-Pst1 and Omp-Pst2 are singular in that they appear to be supported by steric zipper interactions—a structural motif that has, to date, been observed only in prions and amyloid fibers. Steric zippers form from the tight interdigitation of side chains emanating from equivalent residues in short self-matching sequences (4–11 residues) and they are, by nature, highly self-selective. In amyloid and prion assemblies, steric zippers associate β-sheets into highly ordered fibers (18, 19), but the steric zipper interfaces that form between facing monomers of Omp-Pst1 and Omp-Pst2 trimers are single layered. Thus, perhaps, neither Omp-Pst1 nor Omp-Pst2 would, if monomeric, be able to dimerize face-to-face through these motifs.

The steric zipper interfaces differ in the two porins. In Omp-Pst1, the three single-layered steric zipper interfaces are contributed by residues 206-GVVTSE-211 from extracellular loop L5 and would belong to the symmetry class III of steric zippers (face-to-face, up-down) (18) (Fig. 1 *C* and *D*), with a 15° tilt between the two facing β-strands. This interface is reinforced only by weak electrostatic interaction (distance between nonhydrogen atoms ≥3.5 Å) between K28 and D213 from facing extracellular loops L1 and L5, respectively (*SI Appendix*, Fig. S4*A*). The formation of Omp-Pst1 DOT thus appears fully governed by extracellular loop L5. In Omp-Pst2, residues 282-NLGNYG-287 from facing extracellular loops L7 interact via three single-layered nontilted steric zippers that would correspond to the symmetry class I of steric zippers (face-to-face, up-up) (18) (Fig. 1 *G* and *H*). Each steric zipper interface, centered around residues G284 and N285, is complemented by a network of H-bonds which fastens extracellular loops L5, L7, and L8 from facing monomers (Fig. 1*G* and *SI Appendix*, Fig. S5*A*). Of note, Omp-Pst1 features a 290-NLGNGY-295 sequence in its extracellular loop L7, similar to the 282-NLGNYG-287 sequence of Omp-Pst2. However, the L5 β-hairpin protrusion that contributes the 206-GVVTSE-211 steric zipper interface renders L7 inaccessible in Omp-Pst1 (*SI Appendix*, Fig. S1*A*). Nonetheless, N293, equivalent to Omp-Pst2 N285, plays an important role in Omp-Pst1 DOT formation, contributing two H-bonds to Y216 at the base of

the L5 β-hairpin which stabilize the latter and, therefore, the steric zipper interface (*SI Appendix*, Fig. S4*A*).

To evaluate the steric zipper propensity of Omp-Pst1 and Omp-Pst2 segments involved in their dimerization into DOTs, we crystallized the corresponding peptides. For each, we chose the smallest fragment hypothetically involved in the interaction: 206-GVVTSE-211 from Omp-Pst1, and 283-LGNY-286 from Omp-Pst2. Both peptides produced urchinlike microcrystals from which their structures were solved at 1.7 and 1.0 Å resolution, respectively (Fig. 2 and *SI Appendix*, Table S1). The two peptides display canonical cross-β structures, characterized by the in-register stacking of strands into β-sheets and by the mating of these sheets via a steric zipper, perpendicular to the fiber axis. Thus, both 206-GVVTSE-211 and 283-LGNY-286 have a high propensity to form steric zippers (Fig. 2) in isolation of their respective parent proteins. The 3D profile method (20) also identified these segments as highly prone to form steric zippers, with scores of −26.2 and −22.1 kcal/mol, respectively (*SI Appendix*, Fig. S6). They accordingly form fibrils in vitro (*SI Appendix*, Fig. S6 *A* and *B*).

Omp-Pst1 and Omp-Pst2 Self-Interact in Vitro. We investigated whether Omp-Pst1 and Omp-Pst2 can have adhesion properties in vitro. If so, incorporation of either porin into liposomes should lead to proteoliposome aggregation—a process we monitored by dynamic light scattering (DLS). We first examined phosphatidylcholine (PC) liposomes, whose surfaces are neutral at physiological pH. We used the direct-dilution method to incorporate porins into liposomes, enabling real-time monitoring of the process. Using centrifugation on sucrose gradient (21), we confirmed insertion of Omp-Pst1 and Omp-Pst2 into preformed liposomes, and observed that this process is favored at acidic pH (*SI Appendix*, Fig. S7). We then used DLS to monitor the average hydrodynamic radius of the proteoliposome aggregates which form, upon incorporation of Omp-Pst1 or Omp-Pst2 at increasing concentrations, into preformed liposomes (60-nm starting radius). We found that insertion of either porin into liposomes results in a fast (~30 to 45 s) and porin–concentration-dependent aggregation of proteoliposomes (Fig. 3 and *SI Appendix*, Fig. S8*A*). In contrast, incorporation of *E. coli* OmpF into PC liposomes by the same method had

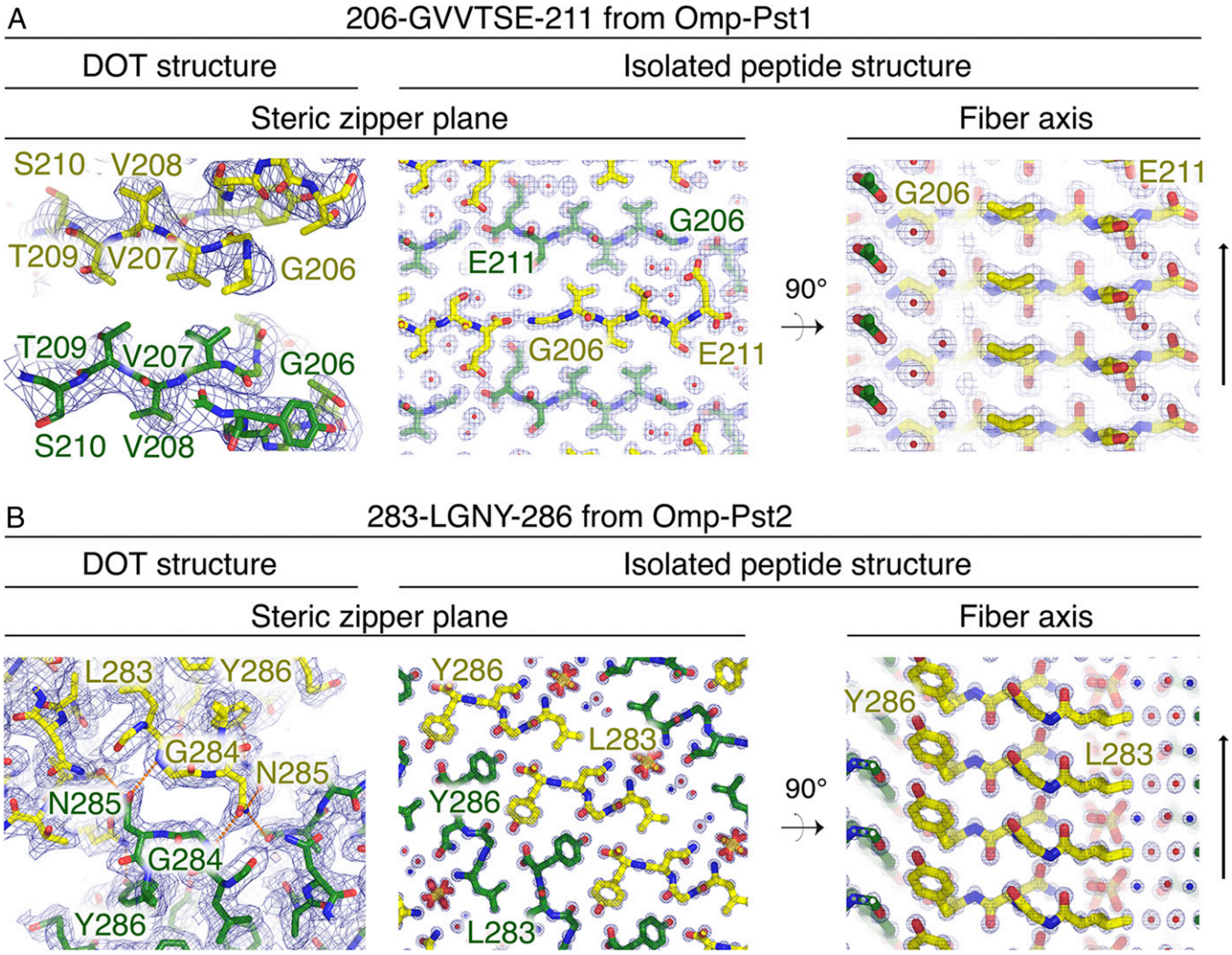

Fig. 2. The segments involved in the formation of the Omp-Pst1 and Omp-Pst2 DOTs also form steric zippers in isolation from their parent protein. (*A* and *B*) Both 206-GVVTSE-211 from Omp-Pst1 (*A*) and 283-LGNY-286 from Omp-Pst2 (*B*) form single-layered steric zippers in the DOT structures of Omp-Pst1 and Omp-Pst2, respectively (*Left*). The 206-GVVTSE-211 and 283-LGNY-286 steric zippers would belong to symmetry classes III and I, respectively. In isolation, the GVVTSE and LGNY peptides also form steric zippers (*Middle* and *Right*), as revealed by their crystal structures solved at 1.7 and 1.0 Å resolution, respectively. (*Middle*) Steric zipper interfaces. (*Right*) A view of 90° apart revealing that both GVVTSE and LGNY adopt a canonical cross-β structure, whereby the steric zipper repeats itself every 4.8 Å through hydrogen bonding along a fiber axis. In the peptide structures, GVVTSE and LGNY form steric zippers that belong to symmetry classes I and III, respectively. Thus, symmetry classes are inversed in the porin and steric zipper structures. In all panels, the corresponding refined 2mFo-DFc electron density map is contoured at 1σ.

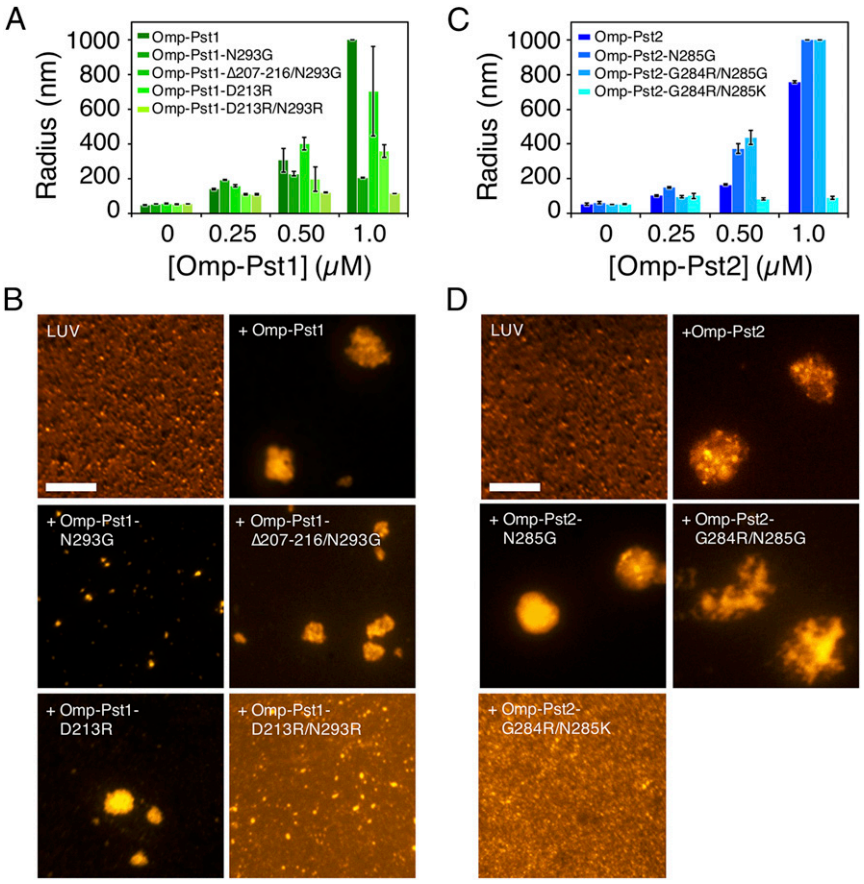

Fig. 3. Altering charge distribution at the DOT interface reduces aggregation properties of Omp-Pst1 and Omp-Pst2 in vitro. (*A*) DLS was used to measure the hydrodynamic radii of proteoliposomes formed 24 h after the addition of increasing concentrations of Omp-Pst1 and its specified mutants (colored in shades of green) to a monodispersed 60-nm liposome solution. (*B*) Proteoliposomes formed at 1 μM porin were spread onto an agarose-coated cover slide for epifluorescence imaging. Large unilamellar vesicles (LUVs) were labeled using rhodamine-derivatized lipids. (*C* and *D*) Same as in *A* and *B*, but for Omp-Pst2. (*B* and *D* scale bars: 20 μm; magnification: 60×.)

comparatively no effect on their average size distribution (*SI Appendix*, Fig. S8*A*). The proteoliposome aggregation induced by Omp-Pst1 and Omp-Pst2 is visible in the pH 4 to 8 range, although it was reduced (smaller liposomes aggregates) at pH 7 and 8, either due to a suboptimal incorporation of porins into liposomes at these pH values or to a reduced self-affinity (*SI Appendix*, Fig. S7). To increase the stringency of further measurements, we nonetheless worked at pH 7, which avoided the formation of proteoliposome aggregates too large (>1 μm) and too polydisperse (>50%) to be resolved by our DLS instrument.

We ascertained the presence of Omp-Pst1 and Omp-Pst2 in proteoliposome aggregates by labeling lipids and porins specifically, and then by examining porin-induced proteoliposome aggregation using epifluorescence microscopy (*SI Appendix*, Fig. S8*B*). Omp-Pst1 and Omp-Pst2 were specifically labeled by engineering of a cysteine (Omp-Pst1-K221C and Omp-Pst2-K211C) at the C-terminal extremity of their L5 loop (*SI Appendix*, Figs. S4*B* and S5*B*, respectively), followed by derivatization of the resulting mutants with a maleimide-coupled green fluorophore (Alexa488). Fluorescent liposomes were prepared by introduction of a red fluorescent lipid (rhodamine derivative) in the bilayer composition. Both Omp-Pst1-K221C and Omp-Pst2-K211C retained the ability to induce proteoliposome aggregation in DLS experiments (*SI Appendix*, Fig. S8*A*). Furthermore, in epifluorescence micrographs, we observed a colocalization of the fluorescence signals arising from the lipids and the porins. The observation that the Omp-Pst1-K221C mutant can still self-associate indicates that the interface revealed by type B crystals is not relevant for proteoliposome aggregation, as the H-bond between K221(NZ) and N293(O) is central to this interface (*SI Appendix*, Fig. S4). Aggregates of proteoliposomes formed at 2 μM porin concentration were examined by transmission electron microscopy, revealing stacks of lipid bilayers (*SI Appendix*, Fig. S9). Those aggregates display periodic order, further exemplifying the strong tendency of Omp-Pst1 and Omp-Pst2 porin to self-associate, both laterally and axially.

Additional DLS data were collected on liposomes composed of palmitoyl-oleyl (PO)PC and PO phosphatidylserine (POPS), in the presence and absence of rough and smooth lipopolysaccharides (LPSs). Data were collected at pH 7, at two liposome concentrations (0.125 and 1.25 mg/mL, corresponding to ∼2 and ∼20 nM of 60-nm liposomes in *SI Appendix*, Figs. S10 and S11, respectively), and at two LPS-to-phospholipid mass ratios (1:10 and 1:100), before and after the removal of the detergent using biobeads.

The data show that *P. stuartii* porin self-association is hindered by electrostatic repulsion between (overall negatively charged) POPS liposomes. Omp-Pst2 self-association is inhibited in the presence of rough and smooth LPSs (*SI Appendix*, Figs. S10 *C* and *D* and S11 *C*–*F*), additional to those already copurified with the protein (*SI Appendix*, Fig. S12 *A* and *B*). Omp-Pst1 self-association is not affected by inclusion of rough LPSs (which lack O-antigen but possess shorter core oligosaccharides and lipid A) in (overall neutral) POPC liposome bilayers, even at an LPS-to-phospholipid mass ratio of 1:10 (*SI Appendix*, Figs. S10 *C* and *D* and S11 *C* and *D*), whereas it is reduced by the inclusion of smooth LPSs (which possess O-antigen,

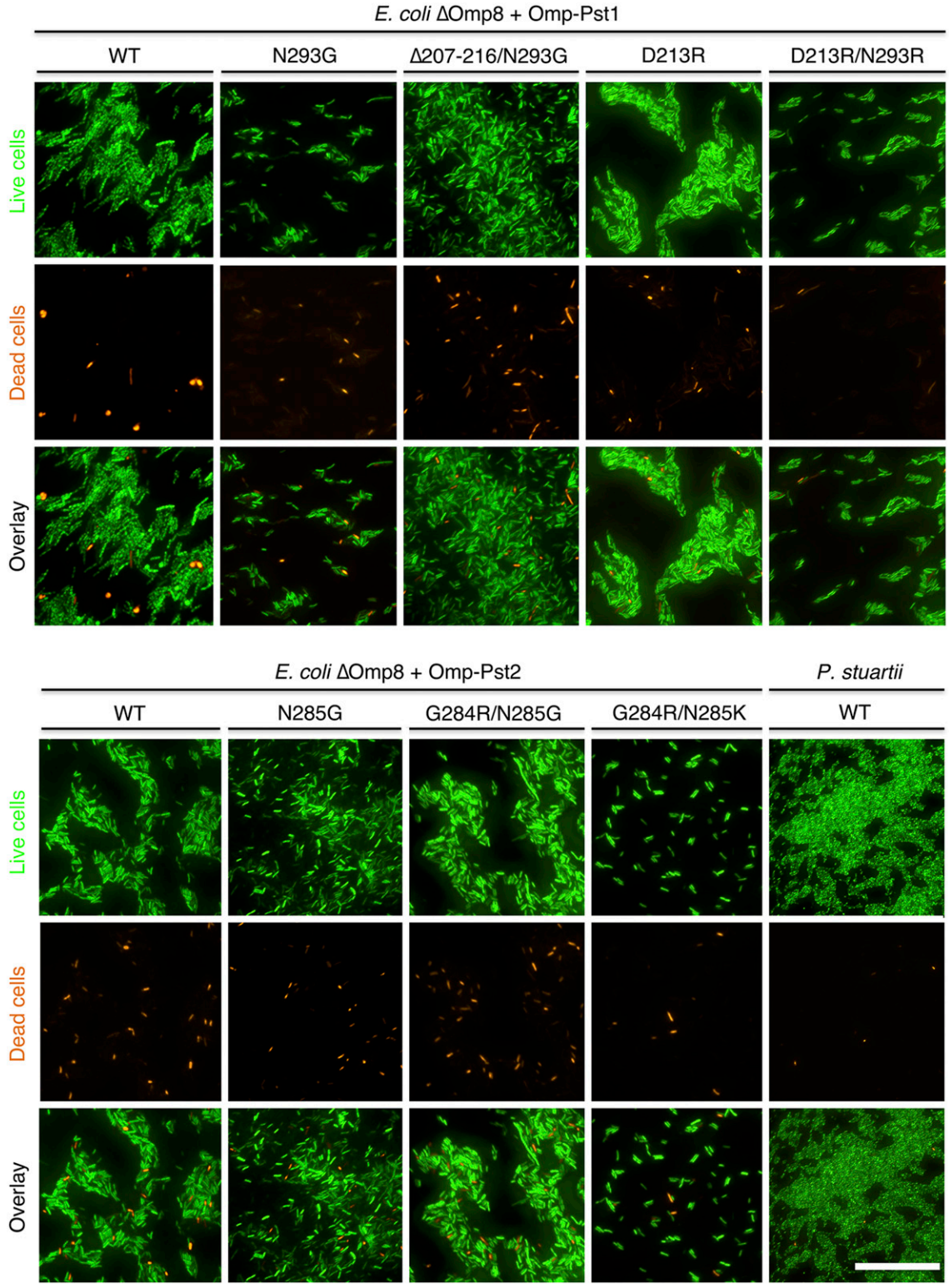

Fig. 4. Omp-Pst1 and Omp-Pst2 mutations affect the formation of floating communities of cells by transformed *E. coli* ΔOmp8 cells. Bacterial strains were grown for 24 h in 96-well plates. Subsequently, live and dead cells were stained with SYTO9 Green and propidium iodide, respectively. Planktonic cells were harvested by direct pipetting from the LB medium, spread on LB-Gelzan, and imaged immediately afterward. For comparison, the floating communities natively formed by *P. stuartii* cells are also shown. (Scale bar: 50 μm for all images; magnification: 60×.)

complete core oligosaccharides, and the lipid A) at an LPS-to-phospholipid mass ratio of 1:100 (*SI Appendix*, Fig. S10 *I* and *J*) and suppressed at 1:10 (*SI Appendix*, Fig. S11 *E* and *F*).

The data also show that detergent does not promote proteoliposome aggregation. First, removal of detergent hardly affects the size of proteoliposome aggregates when phospholipid-only

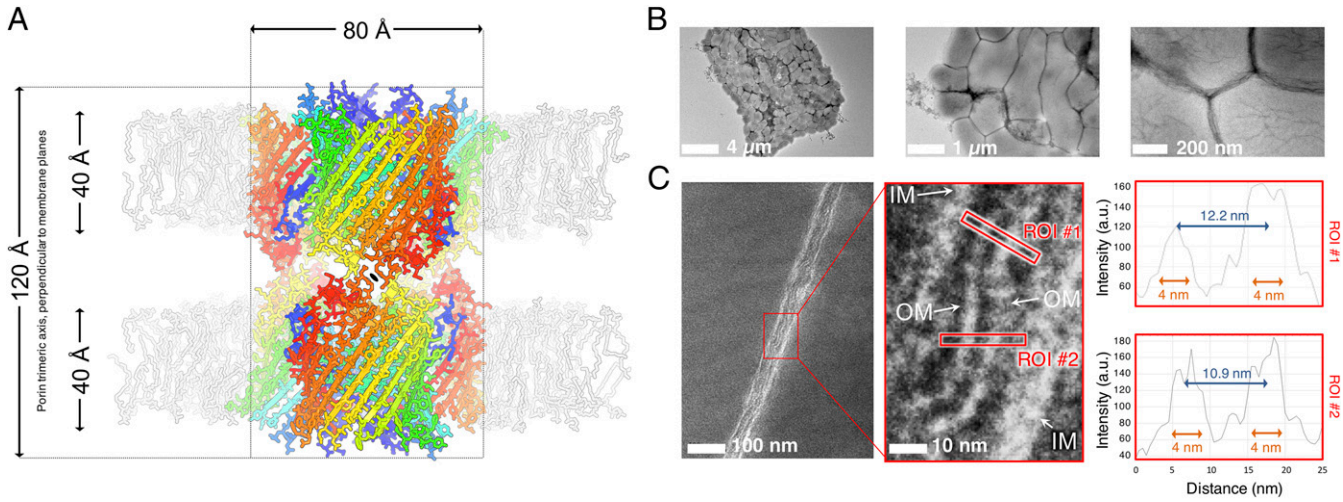

Fig. 5. The distance between adjacent cells in *P. stuartii* floating communities is compatible with the formation of a porin DOT. (*A*) Lateral and longitudinal extent of a porin DOT. The Omp-Pst2 DOT is shown as sticks and ribbons, colored sequence-wise from cold (N-ter) to hot (C-ter) color. A phospholipid bilayer was reconstituted around each trimer in the DOT at the presumed positions of OMs; phospholipids are depicted as gray sticks. (*B* and *C*) Negatively stained transmission electron micrographs of *P. stuartii* floating communities. (*B*) *P. stuartii* floating communities can incorporate hundreds of closely connected cells. Empty spaces with cellular debris are sometimes observed within floating communities, suggesting that cellular death could play a role in the regulation of cell-to-cell contacts of these floating communities. (*C*) A close contact is observed between the OMs of adjacent cells in floating communities (*Left*). In the close-up view (*Middle*), OMs are ∼10 nm apart, a distance that would allow a DOT to form between two OMs. (*Right*) Integrated intensity plots for the two regions of interest (ROIs) highlighted by the red squares depicted in *Middle*. IM, inner membrane.

liposomes are used (*SI Appendix*, Fig. S10 *A*, *B*, *E*, and *F*). Second, the detergent, at concentrations much higher than used in our study, reduces the size of liposomes (*SI Appendix*, *SI Methods* and Fig. S13*A*), whereas incorporation of porins augments it. Additionally, smaller proteoliposome aggregates are observed when higher concentrations of liposomes are used (*SI Appendix*, Figs. S10 and S11 show data at 0.125 and 1.25 mg/mL), supporting the hypothesis that proteoliposome aggregation depends on the number of porins inserted per liposome (*SI Appendix*, Figs. S10 and S11).

We also investigated the effect of high concentrations of salt and chaotropes (urea, NH_4Cl, NaCl, and NaSCN). Efforts to investigate the effects of $CaCl_2$, $MgCl_2$, and $ZnCl_2$ were thwarted by the aggregating effect of these ions on liposomes. We found that Omp-Pst1–induced aggregation of phospholipid-only liposomes is reduced, albeit to different extents, in the presence of urea, NH_4Cl, NaCl, and NaSCN. In contrast, Omp-Pst2–induced aggregation of such liposomes is prevented by urea, promoted by NH_4Cl and NaCl, and unaffected by NaSCN. The presence of LPS changes these patterns, restoring self-association for Omp-Pst1 in the presence of NaCl, although still inhibiting Omp-Pst2 self-association. We note that biobeads and LPSs are incompatible, as LPSs strongly interact with both biobeads and porins, resulting in the extraction of the latter from liposome bilayers (*SI Appendix*, Figs. S10 *C*, *D*, *I*, and *J* and S14). Finally, we used DLS to measure the dissociation constants for lauryldimethylamine *N*-oxide-solubilized Omp-Pst1 and Omp-Pst2 DOTs (*SI Appendix*, *SI Methods* and Fig. S13*B*). Fitting of these data suggests dissociation constants of 0.6 and 0.4 μM for Omp-Pst1 and Omp-Pst2, respectively, at pH 7.

Self-Association of Omp-Pst1 and Omp-Pst2 Is Driven by Electrostatic Interactions. We used site-directed mutagenesis to further characterize self-association of Omp-Pst1 and Omp-Pst2 in vitro. First, we targeted the steric zipper interface observed in Omp-Pst1 DOTs (*SI Appendix*, Fig. S4), either by introduction of point mutations in L5 and L7 (Omp-Pst1-D213R, Omp-Pst1-N293G, and Omp-Pst1-D213R/N293R) or by deletion of the full L5 β-hairpin that supports this interface (Omp-Pst1-Δ207–216/N293G) (*SI Appendix*, Fig. S4*D*). The charge-altering mutations D213R (*SI Appendix*, Fig. S4*E*) and D213R/N293R (*SI Appendix*, Fig. S4*F*) respectively reduced and suppressed the ability of Omp-Pst1 to induce proteoliposome aggregation (Fig. 3 *A* and *B*). The L7 mutant Omp-Pst1-N293G (*SI Appendix*, Fig. S4*C*), designed to destabilize extracellular loop L5—thereby inhibiting steric zipper formation—through suppression of the two H-bonds between N293 and Tyr216, was unable to promote proteoliposome aggregation (Fig. 3 *A* and *B* and *SI Appendix*, Fig. S4). The inability of Omp-Pst1-N293G to induce proteoliposome aggregation was yet fully reversed by deletion of the entire L5 β-hairpin, namely, Omp-Pst1-Δ207–216/N293G (*SI Appendix*, Fig. S4*D*). Hence, the self-association properties of Omp-Pst1 are impacted by electrostatic repulsion or destabilization of the steric zipper interface, but not by the complete suppression of the L5 β-hairpin (Fig. 3 *A* and *B*). Likewise, two Omp-Pst2 mutants aimed at disrupting the 282-NLGNYG-287 steric zipper interface, namely, Omp-Pst2 N285G and Omp-Pst2-G284R/N285G (*SI Appendix*, Fig. S5 *C* and *D*), showed increased ability to induce proteoliposome aggregation (Fig. 3 *C* and *D*). Again, only the Omp-Pst2-G284R/N285K mutant with two positive charges added side-by-side (*SI Appendix*, Fig. S5*E*) displayed a reduced ability to induce proteoliposome aggregation, reminiscent of Omp-Pst1-D213R/N293R. Hence, the main driving force behind Omp-Pst1 and Omp-Pst2 self-association appears to be electrostatic attraction, while single-layered steric zipper interaction between facing monomers could underlie a slotting mechanism that regulates DOT formation. In that case, Omp-Pst1-Δ207–216/N293G should form DOTs that solely assemble through electrostatic interactions, since both steric zipper interfaces available at the surface of Omp-Pst1 should be disrupted in that mutant.

To verify this hypothesis, we crystallized Omp-Pst1-Δ207–216/N293G and solved its structure at 3.2 Å resolution (*SI Appendix*, Fig. S15 and Table S1). Reminiscent of type A Omp-Pst1 crystals, those of Omp-Pst1-Δ207–216/N293G belong to the C2 space group and reveal the presence of a DOT at the unit cell level (*SI Appendix*, Fig. S4 *A* and *B*). The buried surface area per facing trimer is 1,126 $Å^2$, and the dimerization interface delineates a large negatively charged cavity characterized by a volume of 24,540 $Å^3$

(*SI Appendix*, Fig. S15*C*). As proposed, electrostatic interactions between extracellular loops are at the basis of this DOT, which is not supported by steric zipper interactions and wherein facing channels do not join at their extracellular ends—another difference with the DOTs formed by wild-type Omp-Pst1 and Omp-Pst2. Rather, one monomer from each trimer plugs into the center of the facing trimer and establishes contact with the three facing monomers through extracellular loops L7 (to L4 in a first monomer), L8 (to L6 and L8 in a second monomer), and L5 (to L5 in the third monomer). The first two interaction zones are polar, featuring H-bonds between Asp296(OD2) and Met168(N) and between the NZ atom K334 and the main chain carbonyl oxygen of Asp254, respectively (*SI Appendix*, Fig. S15*D*). The unnatural Omp-Pst1-Δ207–216/N293G DOT is nevertheless characterized by a more accessible central cavity, showing reduced surface complementarity between facing trimers (0.37) and featuring six large ellipsoidal fenestrations (up to 7 × 20 Å) (*SI Appendix*, Fig. S15).

Omp-Pst1 and Omp-Pst2 Support Cell-To-Cell Contact in *P. stuartii* Floating Communities. *P. stuartii* is highly social, forming floating communities of cells before depositing as surface-attached biofilms (12). We thus asked whether a correlation would exist between expression of *P. stuartii* porins and the formation of such floating communities. Omp-Pst1 is the major porin of *P. stuartii* (*SI Appendix*, Fig. S12*C*) and essential to its survival; hence, a knockout strategy was unsuited to challenge our hypothesis (12). Rather, we opted for an ectopic expression strategy, using as a surrogate for *P. stuartii* a strain of *E. coli* BL21 deleted of its major porins OmpF, OmpC, OmpA, and LamB: *E. coli* ΔOmp8 (22) (*SI Appendix*, *SI Methods*). Like BL21, the ΔOmp8 strain does not form detectable floating or surface-attached biofilms (*SI Appendix*, Fig. S16). However, this strain displays reduced growth and fitness and a longer lag-phase (*SI Appendix*, Fig. S17*A*). Ectopic expression of either Omp-Pst1 or Omp-Pst2 in ΔOmp8 cells restores normal growth and reduces the lag phase (*SI Appendix*, Fig. S17*A*). Furthermore, it confers to *E. coli* ΔOmp8 cells the ability to form floating communities similar to those formed by *P. stuartii* (Figs. 4 and 5 and *SI Appendix*, Fig. S16). Formation of these is independent of that of surface-attached biofilms, which recombinant ΔOmp8 strains remain unable to form (*SI Appendix*, Fig. S16).

We then set to verify whether mutants unable to induce aggregation of proteoliposomes would also fail at forming floating communities. ΔOmp8 cells expressing mutated versions of Omp-Pst1 (D213R, N293G, D213R/N293R, and Δ207–216/N293G) or Omp-Pst2 (N285G, G284R/N285G, and G284R/N285K) display similar growth and lag phases as cells expressing wild-type Omp-Pst1 and Omp-Pst2, demonstrating that the mutants are well-expressed and folded, and that their diffusive properties are not affected (*SI Appendix*, Fig. S17 *B* and *C*). Strikingly, however, ΔOmp8 cells expressing porin mutants that are able to induce aggregation of proteoliposomes in vitro form floating communities, whereas those expressing mutants unable to self-associate in vitro do not (Figs. 3 and 4). Thus, our data show that the expression of self-associating *P. stuartii* porins is sufficient to enable formation of communities of cells by a non–biofilm-forming *E. coli* strain (Fig. 4 and *SI Appendix*, Fig. S16). We therefore propose that this mechanism is at play in the formation of *P. stuartii* floating communities (Fig. 5), wherein cell-to-cell contacts are observed. As the formation of floating communities precedes that of surface-attached biofilms (12) (Fig. 5 and *SI Appendix*, Fig. S18), porins could also be involved in the cell-to-cell contacts observed within the core of surface-attached biofilms (*SI Appendix*, Fig. S19).

Discussion

The crystallographic structures of Omp-Pst1 and Omp-Pst2 reveal that, within crystals, these porins are able to form DOTs through self-matching interaction of homologous segments in their extracellular loops (Figs. 1 and 2). Using liposome-based assays, we found that Omp-Pst1 and Omp-Pst2 display self-association properties in vitro (Fig. 3), while by means of ectopic expression in ΔOmp8 (a porin-devoid strain of *E. coli*), we showed that the sole expression of Omp-Pst1 or Omp-Pst2 endows these model cells with the capability to form floating communities (Fig. 4). Thus, our data suggest that the self-association of porins from adjacent cells can sustain contact between these cells. Based on buried surface area statistics, the DOTs revealed by type A crystals of Omp-Pst1 and by crystals of Omp-Pst2 and Omp-Pst1-Δ207–216/N293G are compatible with the adhesive properties of these porins, but the side-by-side DOTs observed in type B crystals of Omp-Pst1 are not. We thus propose that the DOT structures are the biological assemblies that contribute to rivet cells one to another in *P. stuartii* floating communities (Fig. 5), possibly in parallel with other adhesion mechanisms. Our observation that DOT formation is impaired by smooth LPSs suggests that DOTs may be specific to "rough" colonies.

Floating communities of cells associated through DOTs could provide a scaffold for biofilm genesis, allowing the building of a critical biomass before deposition onto a surface and secretion of an extracellular matrix. In line with this hypothesis, cells within the core layers of *P. stuartii* surface-attached biofilms (*SI Appendix*, Fig. S19 *A* and *B*) display the same phenotype as those in floating communities; that is, a close contact is observed between their OMs (Figs. 4 and 5 and *SI Appendix*, Fig. S19 *A* and *B*). Hence, Omp-Pst1 and Omp-Pst2 DOTs could be targeted to inhibit socialization of *P. stuartii* in its early stages—that is, before formation of a canonical biofilm, when only cell-to-cell contact is at play. We showed that a simple disruption or removal of the steric zipper interface does not suppress the self-associating properties of the porins, but that they can be abolished in vitro and in vivo through destabilization of the steric zipper interface or by electrostatic repulsion (Figs. 3 and 4). In yeast, steric zippers promote the selection of strains based on self-templating prions, while in amyloid diseases (19), they allow the formation of a variety of fiber polymorphs which differ in toxicity and shape. In *P. stuartii* porins, steric zippers could serve to avoid interspecies DOT formation, thus restricting contact to cells of the same strain only.

Within crystallographic DOTs, facing channels are opened, suggesting that they could provide, in vivo, an effective conduit for the exchange of signaling solutes or nutrients by passive diffusion (Fig. 1)—irrespective of whether or not they are at the origin of the cell-to-cell contact phenotype. It is known that within biofilms, cells exchange chemical information through a mechanism termed "quorum sensing" (QS), which orchestrates the phenotypic adaptation undergone by bacteria as they morph from the planktonic isolated state to the multicellular biofilm state (23). QS is also involved in the adaptation of biofilm cells to local environmental changes (23), in metabolic codependence (24) and time-sharing processes (25), and in the release of cells from the biofilm (23). As yet, however, it had remained unclear how soluble QS effectors could mediate intercellular communication in the first stages of biofilm formation—that is, when the cell density is low and no surrounding matrix is present. The DOT structures hint at a direct intercellular communication mechanism, which would be effective regardless of the cell density or the diffusion volume. Such a mechanism would be well adapted to enable cell cross talk in the floating communities that form before attachment on a surface.

The crystallographic structures show that Omp-Pst1 forms more hermetic DOTs (virtually no fenestrations) than Omp-Pst2, suggesting that intercellular solute translocation would be more efficient across Omp-Pst1 DOTs (Fig. 1 *B* and *F*). Also, the presence of an additional constriction zone in Omp-Pst2 channel would limit large solute exchange across Omp-Pst2 DOTs (Fig. 1 *J* and *K*). Hence, Omp-Pst1 DOTs are better candidates than Omp-Pst2 DOTs for the exchange of signaling solutes (23) and nutrients (24, 25) between *P. stuartii* cells. The structure of maltose-bound Omp-Pst1 is particularly interesting in this context, because it reveals not

only that this porin could be involved in the harvesting of maltose (and other di-glycosides) at the surface of the OM (*SI Appendix*, Fig. S1*B*), but also that the binding site for maltose is not affected by the oligomerization into a DOT. Hence, Omp-Pst1 DOTs could permit equilibration of di-glycoside concentrations between adjacent cells. In contrast, the protrusion contributed by the longer L6 loop of Omp-Pst2 would prevent the binding of a solute at this locus. Furthermore Omp-Pst2 is highly cation selective, and the electrostatic potential developed along its channel is suggestive of a facilitated transport of cations from the periplasm to the bulk (Fig. 1*L*). MD simulations have revealed the propensity of Omp-Pst2 to become nonconductive when cations translocate toward the periplasm, while recent experimental work highlighted the essential role it plays in the resistance to high urea concentrations and the regulation of the cationic content of the periplasm (12). In pathophysiological conditions where *P. stuartii* cells encounter high urea concentrations (2–5), e.g., in the urinary tract, Omp-Pst2 could facilitate the export of the ammonium that accumulates in the periplasm (12) due to *P. stuartii* urease activity (12). Omp-Pst2 DOTs could therefore function as check valves, allowing adjacent cells to expel cationic waste through fenestrations at the dimerization interface, while not reabsorbing it. The observation that Omp-Pst2 self-association is promoted by high concentrations of ammonium chloride is in favor of this hypothesis.

In conclusion, our results suggest a previously uncharacterized role for porins, namely, to form primitive junctions between *P. stuartii* cells. These junctions could foster the formation of floating communities (Figs. 4 and 5) and support intercellular communications. Porin DOTs could thus represent new targets for diagnosis, disruption, and eradication of *P. stuartii* biofilms and associated chronic infections. It remains unclear if biofilm-forming species other than *P. stuartii* also form floating communities before surface-attached biofilms, and, if so, whether or not porin DOTs do support the formation of these floating communities. Examination of porin structures deposited in the Protein Data Bank, and of their crystal-packing interactions, reveals that many crystallize as DOTs associated through their extracellular loops. Thus, some porins may need to be reexamined for their putative propensity to self-associate, in light of the DOTs they form in crystals (e.g., 2j4u, 2xe1, 2xe2, 2xe5, 2y0h, 3poq, 3pou, 3pox, 3t0s, 3t24, 3wi4, 3wi5, 4aui, 4frt, 4fso, 4gey, and 4gf4). Further work will be needed to examine the occurrence of porin DOTs in other gram-negative biofilm-forming bacteria, and the extent to which these DOTs are supported by steric zipper interactions.

Methods

A full description of methods is given in *SI Appendix, Materials and Methods*. Briefly, *E. coli* strain BL21 (DE3) ΔOmp8 (Δ*lamB ompF::Tn5* Δ*ompA* Δ*ompC*) was used to generate recombinant strains. Expression of Omp-Pst1 and Omp-Pst2 in *P. stuartii* and *E. coli* ΔOmp8 strains was monitored using qRT-PCR. Crystallization conditions were screened using standard crystallization screens and improved manually. Porin crystals were grown by the sitting drop method, and peptide crystals by the hanging drop method. X-ray data were collected at European Synchrotron Radiation Facility (ESRF) beamlines ID14-EH4, ID23-EH2, and ID30B; processed and scaled using standard software; and phased either by molecular replacement with homology models or by direct methods. Large unilamellar liposomes were produced by the standard film hydration method and their average hydrodynamic radius was determined using DLS; epifluorescence imaging was performed using an inverted microscope. Floating and surface-attached biofilms of *E. coli* and *P. stuartii* were prepared and imaged by epifluorescence microscopy as described in ref. 12. Electron micrographs of *P. stuartii* floating communities were obtained by sedimentation (30 min) of fixated planktonic cells, followed by negative staining with phosphotungstic acid (Fig. 5) or sodium silicotungstic acid (*SI Appendix*, Fig. S19).

ACKNOWLEDGMENTS. We thank E. Kandiah, D. Cascio, M. R. Sawaya, I. Silman, and J. Zaccaï for critically reading the manuscript; C. Breyton and D. Levy for suggesting on-column delipidation of porins and sucrose gradient experiments, respectively; and A. Martel, A. Le Roy, A. Flayhan, A. Laganowsky, A. Davin-Regli, E. Moiseeva, M. Zhao, G. Schoehn, and T. Vernet for stimulating discussions. We are indebted to I. Snigireva for scanning electron micrographs and to J.-P. Kleman and F. Lacroix for technical support and advice during epifluorescence microscopy experiments. This work used the platforms of the Grenoble Instruct Center [Integrated Structural Biology Grenoble: Unité mixte de service 3518 CNRS–CEA–UGA–European Molecular Biology Laboratory (EMBL)], with support from the French Infrastructure for Integrated Structural Biology (Grant ANR-10-INSB-05-02) and the Grenoble Alliance for Integrated Structural Cell Biology (GRAL) (Grant ANR-10-LABX-49-01) within the Grenoble Partnership for Structural Biology. The electron microscopy facility is supported by the Rhône-Alpes Region, the Fondation de la Recherche Medicale, the Fonds Européen de Développement Régional, the CNRS, the CEA, the UGA, the EMBL, and the Groupement d'Intérêt Scientifique-Infrastrutures en Biologie, Santé et Agronomie. We are grateful to the ESRF for beam time under the long-term projects MX722, MX1464, and MX1583 (IBS beamtime allocation group). We acknowledge financial support from the CEA, the CNRS, the UGA, Agence Nationale de la Recherche Grant ANR-15-CE18-0005-02 (to J.-P.C.), GRAL Grant C7H-LXG11A20-COLLETIER (to J.-P.C.), Laboratory of Excellence "Ion Channel Science and Therapeutics" Grant ANR-11-LABX-0015-01 (to M.V.), and Aix-Marseille University and the Service de Santé des Armées (J.-M.P.). M.E.-K. is supported by a joint CEA-GRAL doctoral fellowship (Grant C7H-LXG11A20-DYNAMOP).

1. Manos J, Belas R (2006) The genera Proteus, Providencia, and Morganella. *Prokaryotes* 6:245–269.
2. McHale PJ, Walker F, Scully B, English L, Keane CT (1981) Providencia stuartii infections: A review of 117 cases over an eight year period. *J Hosp Infect* 2:155–165.
3. Stickler DJ (2008) Bacterial biofilms in patients with indwelling urinary catheters. *Nat Clin Pract Urol* 5:598–608.
4. Warren JW (1986) Providencia stuartii: A common cause of antibiotic-resistant bacteriuria in patients with long-term indwelling catheters. *Rev Infect Dis* 8:61–67.
5. Warren JW (1991) The catheter and urinary tract infection. *Med Clin North Am* 75:481–493.
6. Tran Q-T, et al. (2010) Implication of porins in β-lactam resistance of Providencia stuartii. *J Biol Chem* 285:32273–32281.
7. Bajaj H, et al. (2012) Antibiotic uptake through membrane channels: Role of Providencia stuartii OmpPst1 porin in carbapenem resistance. *Biochemistry* 51:10244–10249.
8. Stock I, Wiedemann B (1998) Natural antibiotic susceptibility of Providencia stuartii, P. rettgeri, P. alcalifaciens and P. rustigianii strains. *J Med Microbiol* 47:629–642.
9. Broomfield RJ, Morgan SD, Khan A, Stickler DJ (2009) Crystalline bacterial biofilm formation on urinary catheters by urease-producing urinary tract pathogens: A simple method of control. *J Med Microbiol* 58:1367–1375.
10. Hollick GE, et al. (1984) Characterization of endemic Providencia stuartii isolates from patients with urinary devices. *Eur J Clin Microbiol* 3:521–525.
11. Mobley HL, Chippendale GR, Tenney JH, Warren JW (1986) Adherence to uroepithelial cells of Providencia stuartii isolated from the catheterized urinary tract. *J Gen Microbiol* 132:2863–2872.
12. El Khatib M, et al. (2017) Providencia stuartii form biofilms and floating communities of cells that display high resistance to environmental insults. *PLoS One* 12:e0174213.
13. Zeth K, Thein M (2010) Porins in prokaryotes and eukaryotes: Common themes and variations. *Biochem J* 431:13–22.
14. Nikaido H (2003) Molecular basis of bacterial outer membrane permeability revisited. *Microbiol Mol Biol Rev* 67:593–656.
15. Song W, et al. (2015) Understanding voltage gating of Providencia stuartii porins at atomic level. *PLOS Comput Biol* 11:e1004255.
16. Ponstingl H, Henrick K, Thornton JM (2000) Discriminating between homodimeric and monomeric proteins in the crystalline state. *Proteins* 41:47–57.
17. Lawrence MC, Colman PM (1993) Shape complementarity at protein/protein interfaces. *J Mol Biol* 234:946–950.
18. Sawaya MR, et al. (2007) Atomic structures of amyloid cross-beta spines reveal varied steric zippers. *Nature* 447:453–457.
19. Eisenberg D, Jucker M (2012) The amyloid state of proteins in human diseases. *Cell* 148:1188–1203.
20. Goldschmidt L, Teng PK, Riek R, Eisenberg D (2010) Identifying the amylome, proteins capable of forming amyloid-like fibrils. *Proc Natl Acad Sci USA* 107:3487–3492.
21. Lévy D, Gulik A, Bluzat A, Rigaud JL (1992) Reconstitution of the sarcoplasmic reticulum Ca(2+)-ATPase: Mechanisms of membrane protein insertion into liposomes during reconstitution procedures involving the use of detergents. *Biochim Biophys Acta* 1107:283–298.
22. Prilipov A, Phale PS, Van Gelder P, Rosenbusch JP, Koebnik R (1998) Coupling site-directed mutagenesis with high-level expression: Large scale production of mutant porins from E. coli. *FEMS Microbiol Lett* 163:65–72.
23. Davies D (2003) Understanding biofilm resistance to antibacterial agents. *Nat Rev Drug Discov* 2:114–122.
24. Liu J, et al. (2015) Metabolic co-dependence gives rise to collective oscillations within biofilms. *Nature* 523:550–554.
25. Liu J, et al. (2017) Coupling between distant biofilms and emergence of nutrient time-sharing. *Science* 356:638–642.